Coherent generation of symmetry-forbidden phonons by light-induced electron-phonon interactions in magnetite

S. Borroni,[1] E. Baldini,[1,2] V. M. Katukuri,[3] A. Mann,[1] K. Parlinski,[4] D. Legut,[5] C. Arrell,[2] F. van Mourik,[2] J. Teyssier,[6] A. Kozlowski,[7] P. Piekarz,[4] O. V. Yazyev,[3] A. M. Oleś,[8] J. Lorenzana,[9] and F. Carbone[1,*]

[1]*Laboratory for Ultrafast Microscopy and Electron Scattering and the Lausanne Centre for Ultrafast Science, IPHYS, École Polytechnique Fédérale de Lausanne, CH-1015 Lausanne, Switzerland*

[2]*Laboratory for Ultrafast Spectroscopy and the Lausanne Centre for Ultrafast Science, ISIC, École Polytechnique Fédérale de Lausanne, CH-1015 Lausanne, Switzerland*

[3]*Chair of Computational Condensed Matter Physics, IPHYS, École Polytechnique Fédérale de Lausanne, CH-1015 Lausanne, Switzerland*

[4]*Institute of Nuclear Physics, Polish Academy of Sciences, 31-342 Kraków, Poland*

[5]*IT4Innovations Center, VSB-Technical University of Ostrava, 17.listopadu 15, 708 33 Ostrava, Czech Republic*

[6]*Department of Quantum Matter Physics, University of Geneva, CH-1211 Geneva, Switzerland*

[7]*Faculty of Physics and Applied Computer Science, AGH-University of Science and Technology, Aleja Mickiewicza 30, PL-30059 Kraków, Poland*

[8]*Marian Smoluchowski Institute of Physics, Jagiellonian University, prof. S. Lojasiewicza 11, PL-30348 Kraków, Poland*

[9]*Institute for Complex Systems–CNR, and Physics Department, University of Rome "La Sapienza," I-00185 Rome, Italy*

(Received 3 March 2017; published 19 September 2017)

Symmetry breaking across phase transitions often causes changes in selection rules and emergence of optical modes which can be detected via spectroscopic techniques or generated coherently in pump-probe experiments. In second-order or weakly first-order transitions, fluctuations of the ordering field are present above the ordering temperature, giving rise to intriguing precursor phenomena, such as critical opalescence. Here, we demonstrate that in magnetite (Fe_3O_4) light excitation couples to the critical fluctuations of the charge order and coherently generates structural modes of the ordered phase above the critical temperature of the Verwey transition. Our findings are obtained by detecting coherent oscillations of the optical constants through ultrafast broadband spectroscopy and analyzing their dependence on temperature. To unveil the coupling between the structural modes and the electronic excitations, at the origin of the Verwey transition, we combine our results from pump-probe experiments with spontaneous Raman scattering data and theoretical calculations of both the phonon dispersion curves and the optical constants. Our methodology represents an effective tool to study the real-time dynamics of critical fluctuations across phase transitions.

DOI: 10.1103/PhysRevB.96.104308

I. INTRODUCTION

Magnetite (Fe_3O_4) is the earliest discovered magnetic material. Nowadays, it is widely used in recording devices and as a catalyst [1,2], and its fast reaction to light excitation holds promise for future applications in oxide electronics [3,4]. At room temperature, the ground state of magnetite is half-metallic ferrimagnetic and the crystalline structure is an inverse cubic spinel, in which tetrahedrally coordinated A sites are occupied only by Fe^{3+} ions, while octahedrally coordinated B sites are occupied by an equal number of nominal valence Fe^{3+} and Fe^{2+} ions. At the Verwey temperature, T_V (=116 K in our sample), important discontinuous structural and electronic modifications take place. In particular, the crystal symmetry lowers from cubic $Fd\bar{3}m$ to monoclinic Cc and the dc conductivity decreases by two orders of magnitude. The insulating state is the result of the long-range charge and orbital order (CO-OO) that emerges among the B sites in the low-temperature (LT) phase.

Originally, Verwey and Anderson postulated a purely electronic mechanism for the transformation [5,6], which implies an alternate occupation of the $a/4$-spaced $(001)_c$ lattice planes (where a is the lattice parameter) by Fe^{2+} and Fe^{3+} ions below T_V, and a random distribution of the latter cations above T_V, allowing for electronic transport. Although the above model proves correct to a first approximation, recently a far more tangled charge and orbital arrangement was refined below T_V, comprised of excess electrons delocalized over chains of three B-type Fe ions, termed trimerons [7–9]. The trimerons are examples of molecular polarons in which the electronic distribution is interrelated with the shortening of the Fe-Fe distances. Interestingly, extensive research on precursors of the phase transition (PT) substantiates the persistence of local dynamical CO-OO in the form of fluctuating trimeron complexes from T_V to room temperature [10–17]. However, the nature of the short-range order in the pretransition region and the relation between the critical correlations which appear gradually above T_V and the discontinuous modifications at T_V remain contentious. Sample-dependent effects on the critical phenomena prevent more general considerations [18,19].

Optical probes, such as reflectivity [20], ellipsometry [4], infrared spectroscopy, and spontaneous Raman scattering [21,22] have disclosed important information on the electronic and structural properties of magnetite relevant to the mechanism of the Verwey transition. Transfers of spectral weight among different energy regions of the optical spectrum are signatures of the strongly correlated nature of magnetite [23], which manifest themselves both in the discontinuous change of the electronic structure at T_V and in the precursor variations

*Corresponding author: fabrizio.carbone@epfl.ch.

which progressively preempt the Verwey transition. The absorption structures below 2.5 eV were generally attributed to interband transitions between Fe 3*d* states, although alternative interpretations were proposed, at variance on whether only *B* or also *A* sites are involved [4,20,24,25]. The appearance of a rich spectrum of additional infrared- and Raman-active modes below T_V reflects the symmetry lowering of the crystal structure which characterizes the Verwey transition [21,22].

The structural transformation of magnetite is a complex process, in which small atomic displacements from the prototype to the distorted structure are the result of the concomitant condensation of multiple phonons of comparable importance, rather than dominant contributions from few critical modes. The details of the distortions accompanying the Verwey transition have been elucidated by means of x-ray and neutron scattering [7,9,26–28]. In particular, below T_V, subsets of modes at the Γ, Δ, X, and W points are frozen into the static deformations of the low-symmetry structure. Verwey and Anderson's scenario, and subsequent Cullen and Callen's theory [29] only account for electron-electron interactions and thus cannot explain the structural transformation. The involvement of the structural degree of freedom in the transition process was first put forward by Yamada, who proposed that the condensation of fluctuations of the charge density coupled to a Δ_5-symmetry phonon is the main driving force for the metal-insulator transition (MIT) [30]. More recent first-principle computations suggest that both the Δ_5 and X_3 modes are the primary order parameters of the structural transformation, and the strong coupling of the X_3 mode with the conduction-band electrons primarily causes the insulating state below T_V [31,32].

In Yamada's model, the modes of the charge density are treated as classical Ising variables and the transformation as an order-disorder process. Therefore, the spectrum of the electronic excitations of the ordering field is essentially a relaxation response centered at zero frequency, whose width is determined by the inverse relaxation time. A radically different model considers a band of quasi-one-dimensional fermionic quasiparticles, generated by the correlations in the system, and interprets the PT in terms of a Peierls instability [33]. In this case, one expects a richer spectrum of electronic excitations, namely, quasiparticle transitions across the Peierls gap and a collective mode arising from amplitude fluctuations of the ordering field at finite frequency [34].

To map the dynamical evolution of the structural modes across the Verwey transition and their interplay with the electronic excitations, we performed out-of-equilibrium optical spectroscopy experiments. *Ab initio* calculations of the phonon dispersion curves in the monoclinic structure allow us to identify the collective modes that are impulsively photoexcited with the X_3 (13.9–15.6 meV), Δ_2 (18.5–19.6 meV), and T_{2g} mode (25.9 meV). Our assignment of the coherent phonons is further complemented by theoretical predictions of the Raman matrix elements (RMEs). The correspondence between data and computations serves as an anchor point to rediscuss the attribution of the optical absorption peaks at low energy. As a by-product, we clarify the origin of the transitions at optical frequencies debated in literature.

Our main result is that the critical fluctuations of the charge-density wave (CDW) couple to specific ionic motions, giving rise to precursor effects above the critical temperature. In particular, in this paper we show that an optical pump pulse can transiently promote time-dependent electron-phonon interactions and generate coherent phonons which, by symmetry, should be forbidden above the charge ordering temperature. The launch of forbidden phonons needs the assistance of fluctuations of the ordered phase, in contrast to previously proposed mechanisms of coherent phonon generation [35,36], in which a time-dependent force acts on the ions without the concurrence of any low-lying mode. On the other hand, our observations are the time-domain analog of the occurrence of forbidden modes above the critical temperature in spontaneous Raman studies of structural PTs [37]. Our results also provide a measure of the amplitude and persistence time of the critical fluctuations above T_V.

II. EXPERIMENTS

A natural single crystal of magnetite was cut and polished along the $(110)_c$ plane. In the Supplemental Material (SM) [38], we report a thorough characterization by means of resistivity and ac magnetic susceptibility experiments, revealing the typical fingerprints of high-quality single crystals.

Figure 1 displays the steady-state optical conductivity of magnetite in the low-energy region, where temperature-dependent changes of the spectral weight take place. As T_V is crossed, an optical gap opens below 0.2 eV, signaling the onset of the insulating phase. Three main features are respectively centered at 0.6, 2, and 5 eV. Based on density functional theory (DFT) calculations [24], Park and co-workers first attributed such features to intersite transitions between *B*-type Fe t_{2g} states, between *A* and *B* sites and the charge transfer (CT) between O 2*p* and Fe 3*d* states, respectively [20]. Advanced DFT+*U* calculations revised the latter assignment, indicating that the absorption feature at 2 eV does not involve *A*-type

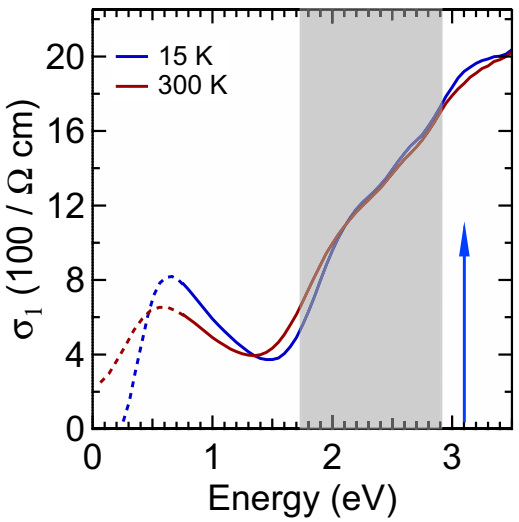

FIG. 1. Steady-state optical properties. Real part of the optical conductivity at 15 and 300 K from the ellipsometry measurements of Ref. [4]. Lines are dashed where curves are extrapolations based on fits to the data. The blue arrow and the shaded area respectively correspond to the energy of the impulsive photoexcitation and the probed range in our time-resolved experiments.

Fe sites, but only B-type Fe sites with different valence states [25]. Nevertheless, no meaningful intensity was predicted for this peak, which makes the assignment put forth in Ref. [25] open for discussion.

In our pump-probe experiments, the photoexcitation energy was tuned to the CT region (3.1 eV) and the probe band spanned the range of the d-d transitions (1.7–2.9 eV). The sample was fixed to the copper cold finger of a closed-cycle He cryostat, with a base pressure of 10^{-8} mbar. The output of an amplified Ti:sapphire laser delivering 50 fs pulses centered at 1.55 eV at a repetition rate of 6 kHz was split into a pump and a probe beam. The pump beam was used to photoexcite the material, after doubling the fundamental frequency in a β-BaB_2O_4 crystal, whereas the probe beam was focused on a CaF_2 crystal to generate broadband pulses from 1.7 to 2.9 eV. The reflectivity spectra were recorded by a fiber-coupled spectrometer. A chopper modulated the train of pump pulses at 3 kHz, so that at every delay time the difference between the pumped and unpumped reflectivity spectrum was measured, yielding a sensitivity down to 10^{-4}. Further details of the setup are described in Refs. [39,40]. The delay time between the two pulses was varied to obtain a sequence of time points representative of the photoinduced dynamics of the material. Spontaneous Raman scattering at 2.4 and 3.1 eV excitation energies was also carried out to discriminate between equilibrium and nonequilibrium effects (see SM for further details [38]).

III. RESULTS

A. Ultrafast broadband spectroscopy

The spectrum of the transient reflectivity as a function of pump-probe delay time, $\Delta R/R\,(E,t)$, at 10 K and $\sim$1 mJ/cm^2 fluence is shown in Fig. 2(a). The $\Delta R/R$ temporal traces averaged over 0.2 eV wide energy intervals are displayed in Fig. 2(b). Damped coherent oscillations lasting over 1.5 ps superimposed to a multiexponential decay clearly emerge in all the time traces of Fig. 2(b) and in the colormap of Fig. 2(a). To analyze these oscillations, the temporal trace averaged between 2.0 and 2.3 eV probe photon energy is fitted with the sum of multiexponential decays and two distinct damped coherent oscillations, convolved with a Gaussian response function. The data and the fitting functions are displayed in Fig. 2(c). The beating between the two oscillations shown in Fig. 2(d) is thereby isolated.

The same fit analysis is repeated at different temperatures and the same fluence. The temperature dependence of all oscillations is displayed in Figs. 3(a)–3(d). Figures 3(e)–3(h) show the evolution of the oscillation amplitude, as obtained by Fourier transforming the time traces. According to the fit results, the energies of the two main modes are respectively in the 13.9–15.6 and 18.5–19.6 meV ranges.

As illustrated in Figs. 3(b) and 3(d), in the cubic phase, $\Delta R/R$ also shows a weak coherent oscillation corresponding to an energy of 25.9 meV, visible in a different spectral range ($<$1.9 eV). Remarkably, although the intensity of the 13.9–15.6 and 18.5–19.6 meV oscillations decreases abruptly above T_V, it does not vanish up to 140 K [see Figs. 3(e) and 3(g)]. Instead, the 25.9 meV oscillation is only visible in the high-temperature (HT) phase and progressively weakens with increasing temperature [see Figs. 3(f) and 3(h)].

Next, in Figs. 4(a)–4(d), we show the dependence of $\Delta R/R$ on the fluence at 120 K, right above the transition temperature. As evidenced in Fig. 4(d), the 13.9–15.6 and 18.5–19.6 meV oscillations are completely quenched with increasing fluence above $\sim$1 mJ/cm^2. In contrast, the intensity of the 25.9 meV oscillation increases with fluence and saturates above $\sim$4 mJ/cm^2.

B. Mode assignment and phonon calculations in $P2/c$ symmetry

To assign these modes, a direct comparison of the Fourier transform (FT) of the coherent oscillations and the spontaneous Raman spectra with the theoretical predictions is carried out in Figs. 5(a)–5(d). The phonon dispersion curves obtained from *ab initio* calculations in the cubic phase below 27 meV are represented by red lines in Fig. 5(c). Figure 5(d) shows the spontaneous Raman spectra at room temperature for 2.4 and 3.1 eV excitation energies, and the FT of the coherent oscillations detected in our pump-probe experiments. The only Raman-active phonon at the zone center in the relevant energy region is the T_{2g} mode.

In the monoclinic phase, the structural PT causes a quadrupling of the unit cell, resulting in new phonon branches, as shown by the blue lines in Fig. 5(b). As a consequence,

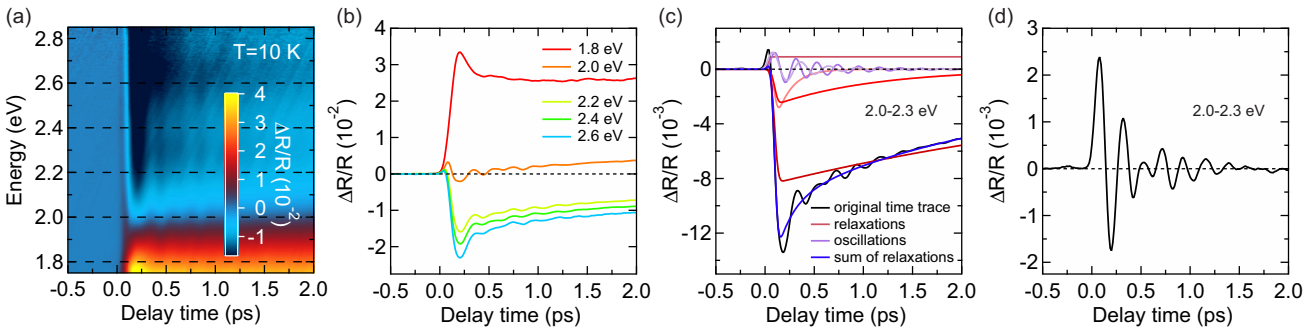

FIG. 2. Response to the impulsive photoexcitation in the monoclinic phase. (a) Color-coded map of differential reflectivity as a function of pump-probe delay time and probe photon energy at 10 K and $\sim$1 mJ/cm^2 fluence. (b) $\Delta R/R$ time traces averaged over 0.2-eV-wide windows centered on the horizontal lines of panel (a). (c) Fit analysis of ΔR/R integrated between 2.0 and 2.3 eV. Fitting functions are displayed in different colors. (**d**) Coherent response isolated through fit analysis of $\Delta R/R$ integrated between 2.0 and 2.3 eV.

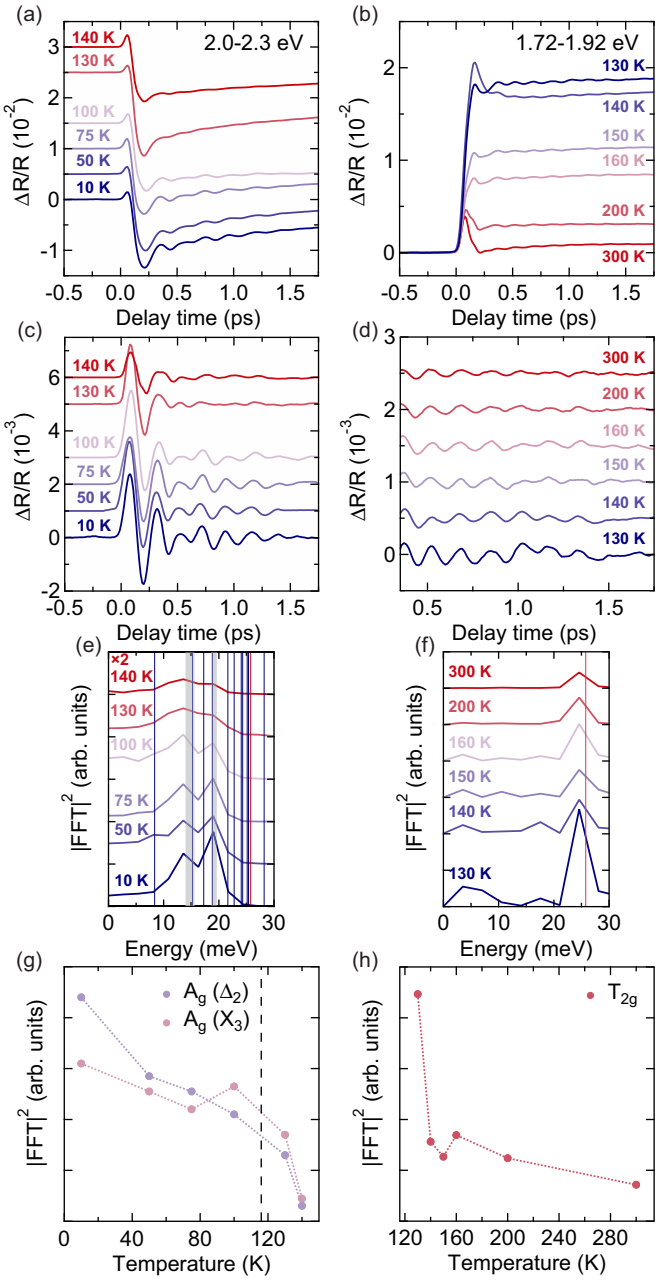

FIG. 3. Temperature dependence of the coherent effects. Left (right) panels refer to the A_g (T_{2g}) modes. (a),(b) Differential reflectivity as a function of pump-probe delay time averaged over 2.0–2.3 and 1.72–1.92 eV energy ranges at different temperatures. (c),(d) Oscillatory component singled out from the time traces of panels (a) and (b) by subtracting the nonoscillatory transient. Since the T_{2g} mode is not the focus of our work, a simple polynomial function was fitted to the incoherent response, after the initial transient. (e),(f) Power spectrum of the coherent response from a Fourier transform (FT) of the oscillatory component. Blue (red) vertical lines indicate the energy of the A_g (T_{2g}) phonon modes at the Γ point in $P2/c$ ($Fd\bar{3}m$) symmetry from *ab initio* calculations. Shaded areas extend over the energy ranges of the beating modes in the LT phase as estimated based on the fit analysis. (g),(h) Temperature dependence of the peak $|\mathrm{FFT}|^2$ corresponding to the oscillations visible by eye. A vertical dashed line denotes T_V.

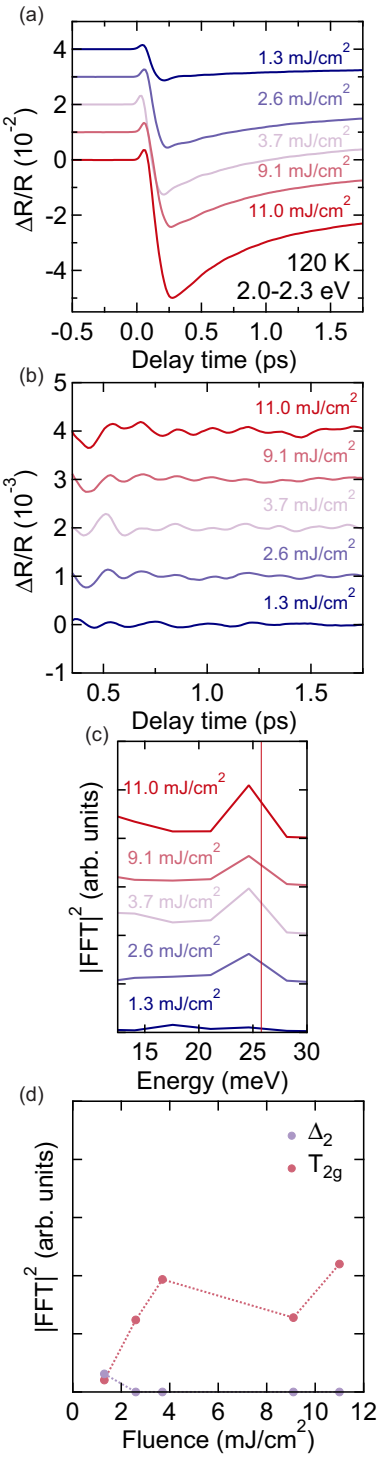

FIG. 4. Fluence dependence of the coherent effects at 120 K. (a) Differential reflectivity as a function of pump-probe delay time averaged in between 2.0 and 2.3 eV at different fluences. (b) Oscillatory component singled out from the time traces of panel (a) by subtracting the nonoscillatory transient. (c) Power spectrum of the coherent response from the FT of the oscillatory component. A red vertical line indicates the energy of the T_{2g} phonon mode at the Γ point in $Fd\bar{3}m$ symmetry from *ab initio* calculations. (d) Temperature dependence of the peak $|\mathrm{FFT}|^2$ corresponding to the oscillations visible by eye.

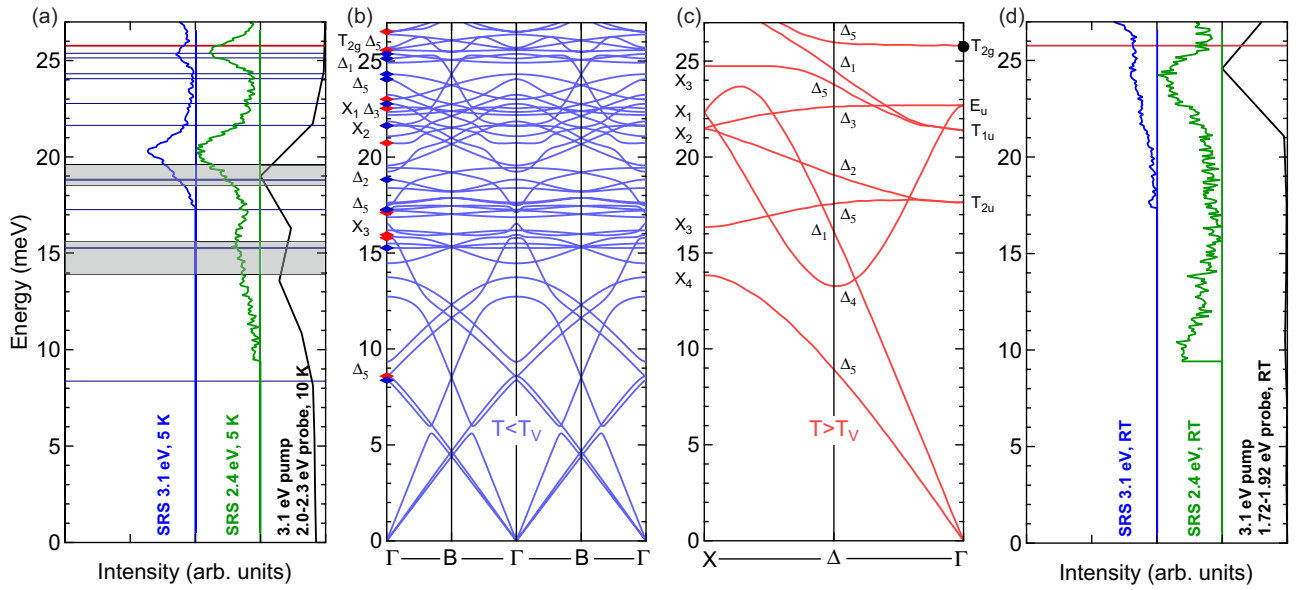

FIG. 5. Assignment of the phonon modes in pump-probe and spontaneous Raman experiments. (a),(d) Comparison between our spontaneous Raman spectra at different excitation energies (colored lines) and $|\mathrm{FFT}|^2$ of the coherent effects in our time-resolved experiments (black line), respectively in the monoclinic and cubic phase. Blue (red) horizontal lines indicate the energy of the A_g (T_{2g}) phonon modes at the Γ point in $P2/c$ ($Fd\bar{3}m$) symmetry from *ab initio* calculations. Shaded areas extend over the energy ranges of the beating modes in the LT phase as estimated based on the fit analysis. (b),(c) *Ab initio* calculations of the phonon dispersion curves, respectively in $P2/c$ and $Fd\bar{3}m$ symmetry. Labels indicate the symmetry of the modes at the Γ, Δ, and X points in $Fd\bar{3}m$ symmetry, and the cubic counterparts of the Raman-active modes at the zone center in $P2/c$ symmetry. Blue (red) diamonds are referred to as A_g (B_g) modes.

various modes are folded to the zone center and become potentially observable by visible-light Raman scattering, as illustrated by the horizontal lines in Fig. 5(a). Figure 5(a) also displays the spontaneous Raman spectra of our single crystal at 5 K for 2.4 and 3.1 eV excitation energies, and their time-resolved counterpart at 10 K. The energy ranges of the coherent oscillations as inferred from the fit analysis are highlighted by shaded areas.

The phonon dispersion curves were calculated in the monoclinic structure (with the approximate symmetry $P2/c$) using the *ab initio* direct method [41,42]. The electronic structure and atomic positions were optimized using the projector augmented-wave [43] and generalized gradient approximation (GGA) [44] implemented in the VASP program [45]. The strong electron interactions in the Fe $3d$ states were included within the GGA+U method [46]. The Hellmann-Feynman forces were calculated by displacing all nonequivalent atoms from their equilibrium positions and the force-constant matrix elements were obtained in the 112-atom supercell. The phonon dispersions along the high-symmetry directions in the reciprocal space were calculated by the diagonalization of the dynamical matrix. The phonon dispersions in the HT cubic phase were studied using the same approach and discussed in Refs. [31,32].

We observed that for crossed pump and probe polarizations the signs of the oscillations visible in the monoclinic phase do not change, in contrast to the behavior typical of B_g-symmetry phonons. Therefore, we rule out the LT B_g modes from the potential candidates for the assignment of these oscillations. On the basis of the comparison presented in Fig. 5, the 13.9–15.6 and 18.5–19.6 meV oscillations are ascribed to the LT A_g modes that are closest in energy, which originate from, respectively, the lowest-energy X_3 and Δ_2 modes in the HT phase. Instead, the 25.9 meV oscillation observed above T_V is unambiguously identified by its energy with the T_{2g} mode of the cubic structure.

Let us note that the peaks in the FT of the coherent oscillations extend in a broad energy range from 11.5 to 21.0 meV. The occurrence of oscillation dephasing and energy renomalization from anharmonic effects may explain the large width of such features and the lower energy of the oscillations compared to their spontaneous Raman counterparts. Our calculations in the approximate symmetry $P2/c$ do not fully account for the effects of CO-OO on the phonon energies, which are thus underestimated, incidentally resulting in a better agreement with the time-resolved data than with the spontaneous Raman spectra.

According to our first-principle computations, the cubic Δ_5 mode gives rise to a monoclinic A_g mode in the energy range intermediate between the 13.9–15.6 and 18.5–19.6 meV oscillations, which may cast doubts on the above assignment based on energy considerations. Such doubts will be dispelled in the following.

C. RME analysis and optical constant calculations in $P2/c$ symmetry

To corroborate our assignments of the oscillations, we benefit from the broadband nature of our optical probe and compare the energy dependence of the experimental RMEs of the oscillations to those obtained from our *ab initio* calculations. Singular value decomposition (SVD) of the $\Delta R/R$ matrix was performed to separate the energy dependence of the incoherent relaxation of the excitations

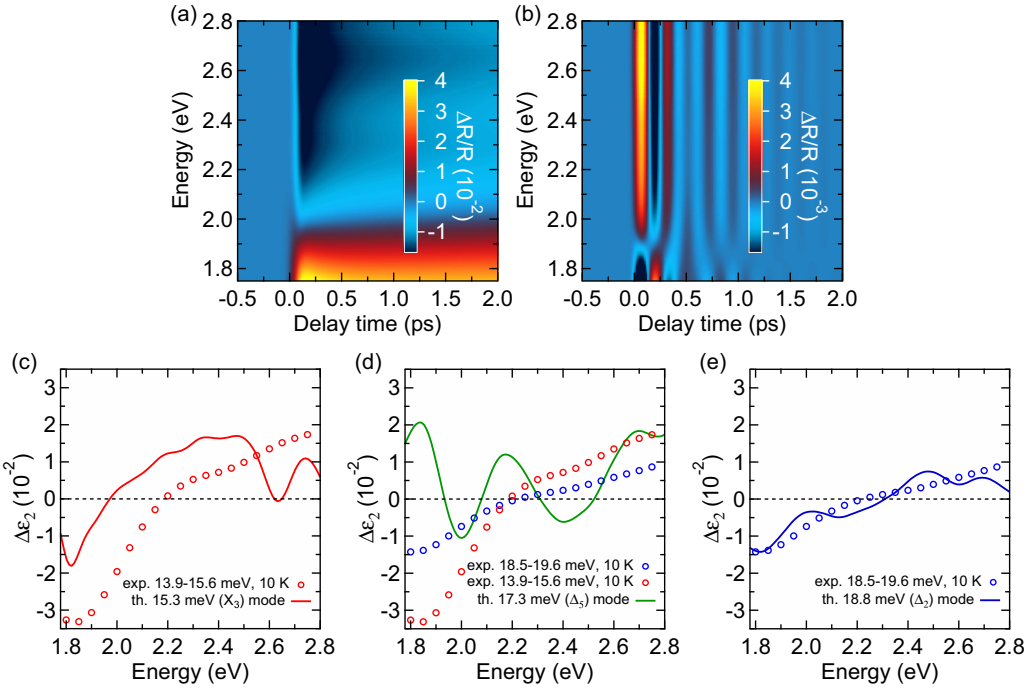

FIG. 6. Time and energy dependence of the coherent response. Reconstruction of the incoherent (a) and the coherent (b) contribution to the $\Delta R/R$ matrix at 10 K and $\sim$1 mJ/cm^2 fluence through our SVD-based method. (c)–(e) Energy profiles of the contributions to the imaginary part of the differential permittivity, $\Delta\varepsilon_2$, from the oscillations at maximum displacement amplitude at 10 K and $\sim$1 mJ/cm^2 (symbols), and calculated RMEs for the A_g modes in the same energy region, in the monoclinic phase (lines). The cubic counterparts of the modes are specified within parentheses. The computed RMEs correspond to maximum atomic displacements of about 5×10^{-2} Å for the 15.3 and 18.8 meV modes and 1×10^{-2} Å for the 17.3 meV mode.

from that of the collective coherent modes corresponding to the oscillations. Qualitative information on the coupling between structural distortions and electronic excitations was thereby gained. Our algorithm decomposed the $\Delta R/R$ matrix into the sum of outer products between orthonormal spectral and temporal vectors, also termed canonical traces, weighted by singular values. The sum was truncated to account only for the physically relevant terms, thus reducing the noise level. The canonical traces were fitted with model functions (see Supplemental Material Fig. 4 [38]). By that, as shown in Figs. 6(a) and 6(b), the incoherent and the coherent contributions to $\Delta R/R$ were reconstructed. The same analysis combined with a fit using a Lorentz model delivered the energy profiles of the differential permittivity associated with the two oscillations at the maximum displacement from the equilibrium positions, depicted in Figs. 6(c)–6(e) and in Fig. 7(b), in a wider energy range. A thorough description and application of our SVD-based method is available in Ref. [39].

To obtain the theoretical RMEs, we followed the procedure described in Ref. [39]. The frequency-dependent dielectric function was calculated for a series of monoclinic unit cells (with approximate symmetry $P2/c$) whose atoms were displaced according to the eigenvectors of the phonon modes in the same 11.5–21.0 meV energy range as the oscillations observed in our experiments. These are the A_g modes of the monoclinic structure that originate from the cubic X_3, Δ_5, and Δ_2 counterparts. We computed the RMEs as the finite differences of the dielectric function associated with the structural distortions in the linear displacement regime. The self-consistent charge density of the electronic ground state was obtained from DFT calculations in the GGA+U approximation implemented in the QUANTUM ESPRESSO package [46,47]. Subsequently, the frequency-dependent dielectric function was calculated with the linear response method within the random phase approximation using the YAMBO package [48] (see the SM for computational details [38]). The computed RMEs depend on the central energies and the widths of the interband transitions. Note that in general, *ab initio* calculations are unable to predict either quantity in an accurate manner. In common practice, to improve the agreement between the experimental optical conductivity and the predictions from first-principle computations, the energy scales are offset by arbitrary constants. Thus, in the following, only a qualitative comparison between our experimental and computed RMEs is possible. Only major features of the computed RMEs such as zero crossings and main peaks are accounted for, with a tolerance margin on the energy locations. Based on our criteria, for on-site Coulomb repulsion, $U = 4$ eV, and Hund's exchange coupling, $J = 1$ eV, our experimental and computed RMEs for the X_3 and Δ_2 modes are in mutual qualitative agreement. In contrast, our theoretical predictions for the Δ_5 mode are completely different from our experimental data for both coherent oscillations. Thus, our RME analysis provides an anchor point to our assignment of the coherent oscillations in the foregoing, following from energy considerations alone.

In addition, as illustrated in Fig. 7(a), our calculations qualitatively reproduce the characteristic features of the

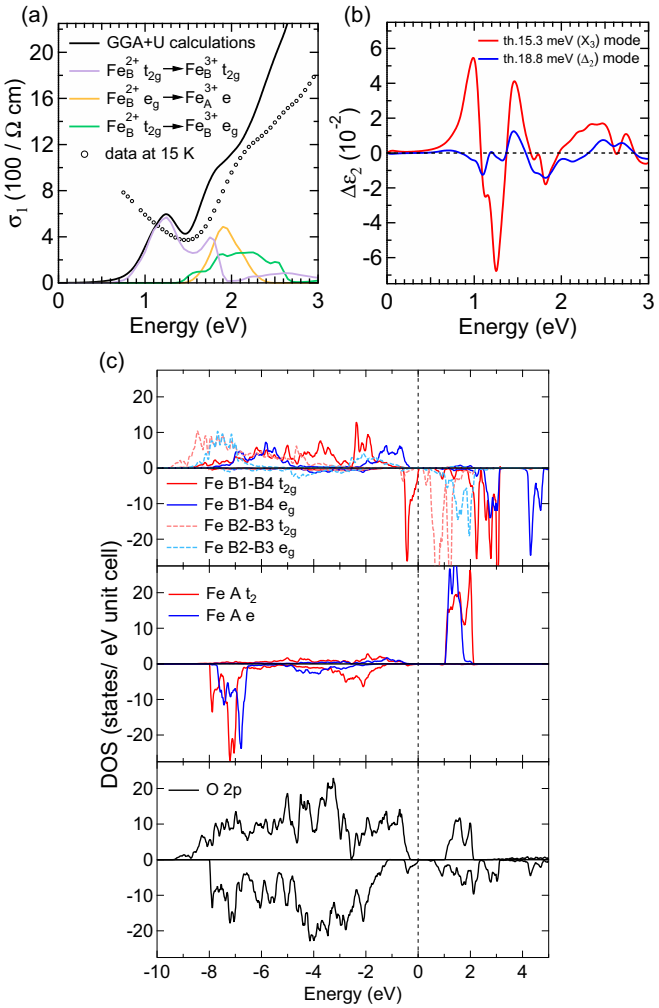

FIG. 7. *Ab initio* calculations of the optical properties. (a) Comparison between the real part of the optical conductivity at 15 K from the ellipsometry measurements of Ref. [4] and the theoretical predictions from our GGA+U calculations with $U = 4$ eV and $J = 1$ eV. The main contributions from different interband transitions to the features around 1.2 and 1.7–2.2 eV are plotted with colored lines and labeled according to the predominant character of the initial and final states. (b) Calculated RMEs for the modes corresponding to the oscillations in the low-energy region below 3 eV. (c) Calculated partial density of states corresponding to inequivalent Fe and O ions in the $P2/c$ subcell. The notation $B1$-$B4$ refers to inequivalent positions in the $P2/c$ subcell (see Ref. [7]). The Fermi level (dashed line) is set to the top of the valence band.

optical conductivity at 15 K, except for the position of the lowest-energy peak. We note that the agreement with the experimental data did not improve for other possible choices of the U parameter (see Supplemental Material Fig. 5 [38]). Considering the reasonable consistency of our predictions to the experimental RMEs in the probed energy range, we reexamine the absorption structure of magnetite in the LT phase to better substantiate the assignment of the interband transitions. As illustrated in Fig. 7(a), the total spectrum was decomposed into the main contributions from different interband transitions (our complete analysis is presented in Supplemental Material Fig. 6 [38]). Individual electronic transitions were discriminated based on the symmetry of the energy bands corresponding to different ions, summarized in Fig. 7(c). Three separate components dominate the debated feature around 2 eV [represented with different colors in Fig. 7(a)], namely, the CT between (i) the minority-spin t_{2g} and e_g states of, respectively, nominal valence Fe^{2+} and Fe^{3+} B sites, (ii) the minority-spin t_{2g} states of the same ions, and (iii) the top of the highest filled band and the bottom of the lowest empty band formed by, respectively, B- and A-type Fe ions in the majority-spin channel. Earlier calculations [25] attributed the peak centered around 2 eV only to the first of the above three excitations purely based on energy considerations, albeit with negligible calculated intensity. In contrast, our assignment relies on the computed spectral weights, which reveal the additional involvement of the A sites. Furthermore, we found that the excitation of the t_{2g} electrons across the band gap extends in the energy region relevant to the 2 eV feature in the form of a satellite peak.

Let us note that RME effects are also responsible for the amplitude changes of the coherent oscillation of the T_{2g} mode as a function of temperature, displayed in the right panels of Fig. 3. The T_{2g} mode is not observable within our detection capability in any spectral region in the monoclinic phase, whereas it resonates in the energy range of positive incoherent response in the cubic phase. The more intense T_{2g} peak observed in spontaneous Raman scattering for 2.4 eV incident light compared to 3.1 eV excitation energy is consistent with the energy dependence of the RME (see Supplemental Material Fig. 3 [38]). The energy range of positive differential reflectivity moves out of our probed spectral region with increasing temperature (see Supplemental Material Fig. 2 [38]). As a consequence, the amplitude of the coherent oscillation of the T_{2g} mode measured in the 1.72–1.92 eV energy range decreases progressively as the temperature is raised away from T_V.

D. CDW-assisted excitation of the LT modes above T_V

Momentum conservation in first-order Raman scattering requires that the phonon modes are at the zone center. Instead, as illustrated in Fig. 5(c), the X_3 and Δ_2 modes are at finite momentum above T_V. Neither of them can be excited by single-mode processes and accordingly they are referred to as *forbidden* modes. Here, we argue that diffusive critical modes at the ordering wave vectors assist the excitation of the forbidden modes above the ordering temperature, T_V. In particular, intrinsic fluctuations of the charge density have been demonstrated to preempt the Verwey transition in the cubic phase of magnetite [11,17]. As pictorially represented in Fig. 8, in our proposed mechanism for the excitation of the forbidden modes above T_V, the above critical fluctuations provide the (0,0,1) and (0,0,0.5) wave-vector contributions (in units of $2\pi/a$) necessary for momentum conservation in a second-order Raman process. In past spontaneous Raman studies of nearly first-order transitions, low-lying modes of precursor order, such as soft phonons, were also suggested to assist the excitation of forbidden modes [37].

We model the light pulses as a time-dependent electric field $\mathbf{E}$, with an oscillation in the range of visible light frequencies, corresponding to the laser central frequency ω_L,

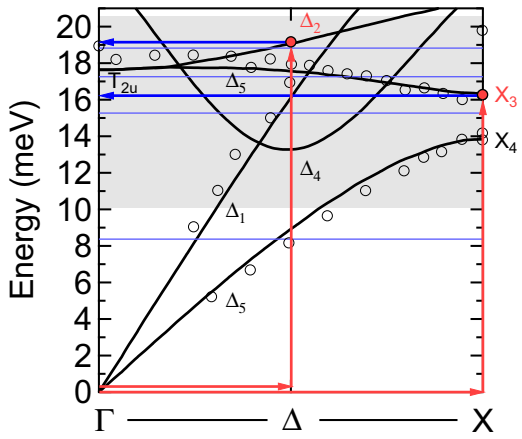

FIG. 8. Two-mode photoexcitation mechanism. Schematic representation of the momentum conservation rule in the photoexcitation mechanism of the X_3, Δ_2, and CDW fluctuation modes above T_V. The phonon dispersion curves in the cubic phase as measured by means of inelastic neutron scattering (symbols) [26] and predicted according to *ab initio* calculations (lines) are shown. The energy and momentum of the phonon and CDW fluctuations are represented by red and blue arrows, respectively. The combination of electronic and vibrational modes allows momentum conservation in the optical process. The shaded area extends over the energy range of the coherent oscillations in the cubic phase, in the vicinity of T_V, as estimated based on a FT analysis.

and a slowly varying modulation $\boldsymbol{\mathcal{E}}$, representing the pulse shape, $\mathbf{E}(t) = \boldsymbol{\mathcal{E}}(t)e^{i\omega_L t}$. We introduce boson creation ($a^\dagger_{\mathbf{q}\lambda}$) and destruction ($a_{\mathbf{q}\lambda}$) operators for phonons of branch λ and momentum $\mathbf{q}$, and the corresponding canonical coordinate, $Q_{\mathbf{q}\lambda} = (\hbar/2\omega_{\mathbf{q}\lambda})^{1/2}(a_{\mathbf{q}\lambda} + a^\dagger_{-\mathbf{q}\lambda})$. The ordering field can be either a bosonic or a classical variable, depending on whether one considers the PT as a Peierls instability, with quantum fluctuation effects [49], or an order-disorder process, described by a ϕ^4 theory, with a central peak-like dynamical response [50].

The time-dependent perturbation introduced by the pump electric field can be expressed by the following two-mode Raman Hamiltonian, which couples CDW fluctuations and a phonon mode, thus acting as a time-dependent electron-phonon interaction controlled by the photoexcitation,

$$H_R = \sum_{\mathbf{q}\lambda} g_{\mathbf{q}\lambda}(t)\rho_{\mathbf{q}} Q_{-\mathbf{q}\lambda} \tag{1}$$

with

$$g_{\mathbf{q}\lambda}(t) = -\frac{V}{4}\boldsymbol{\mathcal{E}}(t)\frac{\partial^2 \boldsymbol{\chi}}{\partial\rho_{\mathbf{q}}\partial Q_{-\mathbf{q}\lambda}}(\omega_L)\boldsymbol{\mathcal{E}}^*(t). \tag{2}$$

Here, $\rho_{\mathbf{q}}$ is the canonical coordinate for the charge fluctuation field with momentum $\mathbf{q}$, V is the sample volume, and $\partial^2\boldsymbol{\chi}/\partial\rho_{\mathbf{q}}\partial Q_{-\mathbf{q}\lambda}$ is the Raman tensor, expressed as the second derivative of the dielectric susceptibility evaluated at the pump frequency, ω_L. Such Raman tensor is a straightforward generalization of those in Refs. [35,40,51]. For simplicity, we assume that bare electron-phonon interactions are already incorporated in the definitions of the field operators, which are quasiparticle operators. For the charge fluctuation field, the derivative can be evaluated with the use of a Lagrange multiplier, as in Ref. [40].

The response produced by the above interaction can be computed as follows, using the Kubo formula, in the response regime linear in fluence,

$$\langle\rho_{\mathbf{q}} Q_{-\mathbf{q}\lambda}\rangle(t) = -\frac{i}{\hbar}\int_{-\infty}^{t} dt'\langle[\rho_{\mathbf{q}}(t)Q_{-\mathbf{q}\lambda}(t), Q_{\mathbf{q}\lambda}(t')\rho_{-\mathbf{q}}(t')]\rangle \times g_{\mathbf{q}}(t'), \tag{3}$$

where $\langle\cdots\rangle$ indicates thermal and quantum averages. If the charge fluctuation field behaves as a classical ordering field, $\rho_{\mathbf{q}}$ can be taken out of the commutator, yielding

$$\langle\rho_{\mathbf{q}} Q_{-\mathbf{q}}\rangle(t) = -\int_{-\infty}^{t} dt'\langle\rho_{\mathbf{q}}(t)\rho_{-\mathbf{q}}(t')\rangle \times \frac{e^{-(t-t')/\tau_{ph}}\sin[\omega_{\mathbf{q}}(t-t')]}{\omega_{\mathbf{q}}} g_{\mathbf{q}}(t'), \tag{4}$$

where τ_{ph} is a phenomenological phonon lifetime and $\omega_{\mathbf{q}}$ is the phonon frequency. For notational simplicity, we drop the phonon branch index λ.

An impulsive form of $g_{\mathbf{q}}(t)$ produces sinelike oscillations of the charge-ion correlation, with an initial strength given by the FT of the squared amplitude of the fluctuations of the ordering field, $\langle\rho_{\mathbf{q}}(0)\rho_{-\mathbf{q}}(0)\rangle$, and an envelope, $\langle\rho_{\mathbf{q}}(t)\rho_{-\mathbf{q}}(t')\rangle$, which carries information on their time correlation. In the case of a step form of $g_{\mathbf{q}}(t)$, the oscillations become cosinelike. Our description represents a generalization of the mechanism proposed in Ref. [36] which can be referred to as fluctuation-assisted stimulated Raman scattering (FASRS).

The launch of the excitations modulates the optical properties through their dependence on the dielectric susceptibility,

$$\delta\boldsymbol{\chi}(\omega,t) = \sum_{\mathbf{q}}\frac{\partial^2\boldsymbol{\chi}}{\partial\rho_{\mathbf{q}}\partial Q_{-\mathbf{q}}}(\omega)\langle\rho_{\mathbf{q}} Q_{-\mathbf{q}}\rangle(t). \tag{5}$$

To apply the FASRS mechanism to the present case, we assume a CDW instability occurring at the X point of the Brillouin zone (BZ), corresponding to a charge stacking along the z direction, described by $\cos(2\pi z/a)$, which yields a charge occupancy (with respect to the average) $-\delta$, 0, δ, 0 for the B-type Fe planes separated by $a/4$. One can additionally consider CDW fluctuations with twice the periodicity, which can assist the launch of modes at the Δ point of the BZ, and can be described with the same method.

The dominant CO in real space, with wave vector $\mathbf{Q} = (0,0,2\pi/a)$, corresponding to the X point of the BZ, can be described as

$$\delta\rho(\mathbf{r}) = \phi_1(\mathbf{r})\cos(\mathbf{Q}\cdot\mathbf{r}) + \phi_2(\mathbf{r})\sin(\mathbf{Q}\cdot\mathbf{r}).$$

The trigonometric factors account for the rapidly varying components of the CO. Instead, (ϕ_1,ϕ_2) designate the real, smoothly varying components of the CO, in the following referred to as the ordering field itself. Energy expansion in a power series of the ordering field and its gradients yields a coarse-grained Landau energy functional, which describes the PT in a phenomenological framework [50].

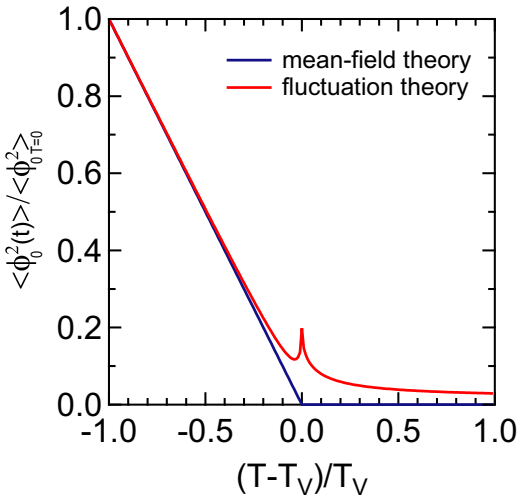

FIG. 9. Temperature dependence of the normalized equal-time correlation of the ordering field across the ordering temperature. The plotted curves refer to a one-component ϕ^4 model at the Gaussian level. The results for a two-component model are qualitatively similar, but the details depend on the interactions among the modes. In these units, the intensity of the anomaly at T_V is regulated by the inverse Ginzburg length [50].

Close to the ordering temperature, the critical fluctuations of the charge density are strongly peaked at the critical wave vector $\mathbf{Q}$ and we can approximate the smooth momentum-dependent quantities in Eq. (5) to their value at the same point. The response reads,

$$\delta\chi(\omega,t) = -\frac{\partial^2\chi}{\partial\rho_{\mathbf{Q}}\partial Q_{-\mathbf{Q}}}(\omega)\frac{N^2}{2}\int_{-\infty}^{t} dt' \sum_{\alpha=1,2}\langle\phi_{\alpha 0}(t)\phi_{\alpha 0}(t')\rangle \times \frac{e^{-(t-t')/\tau_{ph}}\sin[\omega_{\mathbf{Q}}(t-t')]}{\omega_{\mathbf{Q}}} g_{\mathbf{Q}}(t') \quad (6)$$

with N the number of sites and $\langle\phi_{\alpha 0}(t)\phi_{\alpha 0}(t')\rangle$ the autocorrelation of the ordering field at $\mathbf{r}=0$. In the Landau theory, the fluctuations are neglected, and thus the autocorrelation reduces to a time-independent quantity, $\langle\phi_{\alpha 0}^2\rangle$, identical to the squared order parameter, $\langle\phi_{\alpha 0}\rangle^2$, which by definition is different from zero only below T_V (see the blue line in Fig. 9). This corresponds to the notion that the modes become active in the broken-symmetry phase upon folding from the boundary to the center of the BZ.

If the fluctuations are taken into account, the results are different. The equal-time correlation, $\langle\phi_{\alpha 0}^2(t)\rangle$, determines the initial amplitude of the oscillations, as plotted with a red line in Fig. 9 based on calculations at the Gaussian level. This shows that the fluctuations make the modes active even above T_V.

Furthermore, if the coherence time of the oscillations is shorter than the phonon lifetime, it means that the decay is dominated by the factor $\langle\phi_{\alpha 0}(t)\phi_{\alpha 0}(t')\rangle$ in Eq. (6) and one obtains information on the dynamics of the ordering field. For a weakly first-order transition, as in the present case, we expect a small jump of the intensity at the critical point, but a qualitatively similar behavior.

IV. DISCUSSION

In general, the Verwey transition in magnetite is regarded to as a weakly first-order transition. In high-quality natural single crystals, such as our sample, disorder associated with defect content causes phase coexistence around T_V, which, however, comprises a narrow temperature range (see Supplemental Material Fig. 1 [38]). Our proposed scenario in which critical fluctuations assist the excitation of forbidden modes is conceptually different from phase coexistence. Reports of local correlations of precursor order on a finite time scale in the cubic phase of magnetite were presented before. In particular, diffuse scattering of neutrons and x rays is a signature of fluctuations of trimeron complexes sustained above T_V [11,12,17]. Furthermore, the coupling between the dynamics of the charge density and the transverse-acoustic phonons is reflected in the linewidth anomalies of the phonon modes observed by means of inelastic x-ray scattering [16]. To date, the role of imperfections on the degree and character of precursor order is controversial. However, the occurrence of the above effects in highly stoichiometric synthetic crystals points to phenomena intrinsic to the ideal mechanism of the Verwey transition and not sample dependent. In any case, it would certainly be interesting to investigate the effects of disorder on the excitation of the forbidden modes above T_V in spontaneous Raman experiments.

Within the above framework, the excitation and detection of two modes of the monoclinic structure above the critical temperature in our pump-probe experiments can be rationalized considering the effects of critical fluctuations and provide information on their dynamics. Equations (4) and (6) express the fact that, in the presence of a long-lived CDW fluctuation, a lattice vibration with finite momentum can be excited by light, with a coherence time limited by the persistence time of the CDW fluctuation. Practically, the frequencies of the coherent oscillations do not present any meaningful change across the critical region. Accordingly, our results clarify that the charge ordering fluctuations in the pretransition region are comprised of a relaxation response, consistent with Yamada's interpretation of the Verwey transition in terms of a concomitant order-disorder and displacive transformation [30]. Instead, if a Peierls-like mechanism played a significant role in the Verwey transition, the fluctuations of the ordering field would consist of periodic amplitude and phase modulations of the charge density, both in space and time, and accordingly possess finite frequencies. For example, for an electronic spectrum of the critical modes approximated to a single pole at ω_{CDW}, second-order Raman scattering is supposed to give rise to Stokes and anti-Stokes oscillations at $\omega_{\mathbf{Q}} \pm \omega_{CDW}$ with sizable energy modifications as a function of temperature, in sharp contrast to our observations.

By means of our SVD algorithm, we were able to determine the experimental profiles of the RMEs as a function of probe photon energy. A comparison with *ab initio* calculations allowed us to unambiguously identify the modes. This assignment methodology has the advantage to rely on the phonon eigenvector instead of the phonon energy, thus providing precise and specific information.

Our time-resolved experiments directly access the decay time of the coherent oscillations. According to Eq. (6), this is limited by the phonon lifetime τ_{ph} or the persistence time of the CDW fluctuations—whatever is shorter. If the fluctuations of the ordering field are the limiting factor, we expect that the line shapes of the modes in the energy domain become broader above the critical temperature, as is indeed the case [see Fig. 3(e)]. Preliminary results from our inelastic neutron scattering [52] and spontaneous Raman scattering experiments (see Supplemental Material Fig. 3 [38]) indicate that the phonon lifetimes (>600 fs) are significantly longer than the time constants of the coherent oscillations in accord with this result. Therefore, our measurements provide an estimate of the relaxation time of the fluctuations of the order parameter in the 130–140 K pretransition region, $\tau_{CDW} \sim 240$ fs.

Gaussian fluctuations result in a cusp anomaly of the oscillation amplitude at the critical temperature (see Fig. 9). Unfortunately, our temperature and energy resolution are not high enough to test this hypothesis. In any case, the persistence of fluctuations above the ordering temperature [see Fig. 3(g)] is in qualitative agreement with the prediction of the fluctuation model. As illustrated in Fig. 4, fluences above ~ 1 mJ/cm^2 are high enough to suppress the coherent oscillations of the forbidden modes in the critical region, as a result of the rapid decrease of coherence time and length of the fluctuations with increasing temperature away from the ordering temperature. In contrast, the coherent oscillation of the zone-center T_{2g} mode is excited through first-order Raman scattering. Thus, the conventional processes of transient stimulated Raman scattering [35,36] cause the increase of the oscillation amplitude in a linear regime below ~ 4 mJ/cm^2, followed by saturation at higher fluences.

In contrast to our nonequilibrium experiments, in our spontaneous Raman measurements at 2.4 and 3.1 eV excitation energies, no forbidden mode was detected below 27 meV in the disordered phase (see Supplemental Material Fig. 3 [38]). Note that, as mentioned in the foregoing, the spontaneous Raman analog of the effects observed in our pump-probe experiments was reported in structural PTs [37]. The absence of forbidden modes in our spontaneous Raman measurements is indicative of the different sensitivity of the two techniques to low-energy modes, but could also suggest that nonlinear effects enhance the coherent response in our pump-probe experiments. One can easily check that the time-dependent electron-phonon interaction promotes a transient stabilization of the ordered phase, which is equivalent to an increase of the effective ordering temperature in steady-state conditions. Possibly, the above effect amplifies the coherent response, by inducing a breaking of symmetry limited in time and confined in space. Experimentally, to validate this hypothesis, one would need to carry out a thorough study of the fluence dependence of the coherent response in the proximity of the critical temperature. Such an experiment requires accurate temperature control across the specific heat anomaly in the critical region and high enough signal-to-noise ratio to detect small oscillations at low fluences.

V. CONCLUSIONS

Typically, ultrashort laser pulses are used to melt the order parameter of the low-symmetry phase and thus establish the electronic and structural properties of the disordered phase [3,4]. Here, we discussed a more subtle effect, with implications on the coherent control of transition-metal oxides. In particular, we demonstrated that impulsive photoexcitation at 3.1 eV, above the energy onset for O $2p$–Fe $3d$ CT transitions, transiently promotes the coupling between lattice vibrations at finite momentum and fluctuations of the electronic ordering field above the ordering temperature of the Verwey transition in magnetite. In particular circumstances, the optical control of the electron-phonon interactions may even induce order.

Fluctuations of the ordering field are not easy to measure and often require neutron-scattering techniques, generally limited in energy resolution. We developed a method able to probe the dependence of the amplitude and persistence time of critical fluctuations on temperature and light excitation. Our method demonstrated the capability to gain insight into the critical softening of fluctuations in correspondence of PTs. Moreover, our approach enabled us to describe the atomic motions associated with the critical fluctuations and their interplay with the electronic degree of freedom. This further elucidated the microscopic mechanism of the MIT and the interpretation of the optical response of magnetite.

ACKNOWLEDGMENTS

We acknowledge D. Fausti, H. Lee, A. B. Kuzmenko, and D. McGrouther for useful discussions, M. Prester and D. Drobac (Institute of Physics, Zagreb) for the ac susceptibility characterization, and A. Pisoni (Laboratory of Physics of Complex Matter, École Polytechnique Fédérale de Lausanne, Lausanne) for the resistivity characterization. Work at LUMES was supported by NCCR MUST and by the ERC starting Grant No. USED258697. J.L. acknowledges financial support by Italian MIUR under Projects FIRB-HybridNanoDev-RBFR1236VV, PRIN-RIDEIRON-2012X3YFZ2, Premiali-2012 AB-NANOTECH, and Italian MAECI under collaborative Projects SUPERTOP-PGR04879 and AR17MO7. V.M.K. and O.V.Y. acknowledge the support from ERC project "Topo-Mat" (Grant No. 306504). First-principles calculations have been performed at the Swiss National Supercomputing Centre (CSCS) under Project No. s675. A.M.O. and P.P. acknowledge the support by Narodowe Centrum Nauki (NCN, National Science Centre, Poland), Project No. 2012/04/A/ST3/00331. D.L. acknowledges the project "IT4Innovations National Supercomputing Center-LM2015070" and Grant No. 17-27790S of the Grant Agency of the Czech Republic.

[1] A. S. Hoagland, History of magnetic disk storage based on perpendicular magnetic recording, IEEE Trans. Magn. **39**, 1871 (2003).

[2] A. Hu, G. T. Yee, and W. Lin, Magnetically recoverable chiral catalysts immobilized on magnetite nanoparticles for asymmetric hydrogenation of

aromatic ketones, J. Am. Chem. Soc. **127**, 12486 (2005).

[3] S. De Jong, R. Kukreja, C. Trabant, N. Pontius, C. Chang, T. Kachel, M. Beye, F. Sorgenfrei, C. Back, B. Bräuer *et al.*, Speed limit of the insulator–metal transition in magnetite, Nat. Mater. **12**, 882 (2013).

[4] F. Randi, I. Vergara, F. Novelli, M. Esposito, M. Dell'Angela, V. Brabers, P. Metcalf, R. Kukreja, H. A. Dürr, D. Fausti *et al.*, Phase separation in the nonequilibrium Verwey transition in magnetite, Phys. Rev. B **93**, 054305 (2016).

[5] E. Verwey, Electronic conduction of magnetite (Fe_3O_4) and its transition point at low temperatures, Nature (London) **144**, 327 (1939).

[6] P. W. Anderson, Ordering and antiferromagnetism in ferrites, Phys. Rev. **102**, 1008 (1956).

[7] J. P. Wright, J. P. Attfield, and P. G. Radaelli, Long Range Charge Ordering in Magnetite Below the Verwey Transition, Phys. Rev. Lett. **87**, 266401 (2001).

[8] K. Yamauchi, T. Fukushima, and S. Picozzi, Ferroelectricity in multiferroic magnetite Fe_3O_4 driven by noncentrosymmetric Fe^{2+}/Fe^{3+} charge-ordering: First-principles study, Phys. Rev. B **79**, 212404 (2009).

[9] M. S. Senn, J. P. Wright, and J. P. Attfield, Charge order and three-site distortions in the Verwey structure of magnetite, Nature (London) **481**, 173 (2012).

[10] Y. Fujii, G. Shirane, and Y. Yamada, Study of the 123-K phase transition of magnetite by critical neutron scattering, Phys. Rev. B **11**, 2036 (1975).

[11] S. Shapiro, M. Iizumi, and G. Shirane, Neutron scattering study of the diffuse critical scattering associated with the Verwey transition in magnetite (Fe_3O_4), Phys. Rev. B **14**, 200 (1976).

[12] Y. Yamada, N. Wakabayashi, and R. M. Nicklow, Neutron diffuse scattering in magnetite due to molecular polarons, Phys. Rev. B **21**, 4642 (1980).

[13] H. Schwenk, S. Bareiter, C. Hinkel, B. Lüthi, Z. Kakol, A. Koslowski, and J. Honig, Charge ordering and elastic constants in $Fe_{3-x}Zn_xO_4$, Eur. Phys. J. B **13**, 491 (2000).

[14] M. M. Seikh, C. Narayana, P. A. Metcalf, J. M. Honig, and A. K. Sood, Brillouin scattering studies in Fe_3O_4 across the Verwey transition, Phys. Rev. B **71**, 174106 (2005).

[15] R. Řezníček, V. Chlan, H. Štěpánková, P. Novák, and M. Maryško, Magnetocrystalline anisotropy of magnetite, J. Phys.: Condens. Matter **24**, 055501 (2012).

[16] M. Hoesch, P. Piekarz, A. Bosak, M. Le Tacon, M. Krisch, A. Kozłowski, A. M. Oleś, and K. Parlinski, Anharmonicity Due to Electron-Phonon Coupling in Magnetite, Phys. Rev. Lett. **110**, 207204 (2013).

[17] A. Bosak, D. Chernyshov, M. Hoesch, P. Piekarz, M. Le Tacon, M. Krisch, A. Kozłowski, A. M. Oleś, and K. Parlinski, Short-Range Correlations in Magnetite Above the Verwey Temperature, Phys. Rev. X **4**, 011040 (2014).

[18] J.-E. Lorenzo, C. Mazzoli, N. Jaouen, C. Detlefs, D. Mannix, S. Grenier, Y. Joly, and C. Marin, Charge and Orbital Correlations at and above the Verwey Phase Transition in Magnetite, Phys. Rev. Lett. **101**, 226401 (2008).

[19] J. García, G. Subías, J. Herrero-Martín, J. Blasco, V. Cuartero, M. C. Sánchez, C. Mazzoli, and F. Yakhou, Reexamination of the Temperature Dependences of Resonant Reflections in Highly Stoichiometric Magnetite, Phys. Rev. Lett. **102**, 176405 (2009).

[20] S. K. Park, T. Ishikawa, and Y. Tokura, Charge-gap formation upon the Verwey transition in Fe_3O_4, Phys. Rev. B **58**, 3717 (1998).

[21] L. V. Gasparov, D. B. Tanner, D. B. Romero, H. Berger, G. Margaritondo, and L. Forro, Infrared and Raman studies of the Verwey transition in magnetite, Phys. Rev. B **62**, 7939 (2000).

[22] M. B. Yazdi, K. Choi, D. Wulferding, P. Lemmens, and L. Alff, Raman study of the Verwey transition in magnetite thin films, New J. Phys. **15**, 103032 (2013).

[23] P. F. Maldague, Optical spectrum of a Hubbard chain, Phys. Rev. B **16**, 2437 (1977).

[24] Z. Zhang and S. Satpathy, Electron states, magnetism, and the Verwey transition in magnetite, Phys. Rev. B **44**, 13319 (1991).

[25] I. Leonov, A. N. Yaresko, V. N. Antonov, and V. I. Anisimov, Electronic structure of charge-ordered Fe_3O_4 from calculated optical, magneto-optical Kerr effect, and O K-edge x-ray absorption spectra, Phys. Rev. B **74**, 165117 (2006).

[26] E. Samuelsen and O. Steinsvoll, Low-energy phonons in magnetite, Phys. Status Solidi B **61**, 615 (1974).

[27] M. Iizumi, T. Koetzle, G. Shirane, S. Chikazumi, M. Matsui, and S. Todo, Structure of magnetite (Fe_3O_4) below the Verwey transition temperature, Acta Crystallogr. Sect. B: Struct. Crystallogr. Cryst. Chem. **38**, 2121 (1982).

[28] J. Blasco, J. García, and G. Subías, Structural transformation in magnetite below the Verwey transition, Phys. Rev. B **83**, 104105 (2011).

[29] J. R. Cullen and E. Callen, Collective electron theory of the metal-semiconductor transition in magnetite, J. Appl. Phys. **41**, 879 (1970).

[30] Y. Yamada, C. Graham, Jr., G. Lander, and J. Rhyne, *Charge Ordering and Lattice Instability in Magnetite*, *AIP Conf. Proc.* No. 24 (AIP, Melville, NY, 1975), p. 79.

[31] P. Piekarz, K. Parlinski, and A. M. Oleś, Mechanism of the Verwey Transition in Magnetite, Phys. Rev. Lett. **97**, 156402 (2006).

[32] P. Piekarz, K. Parlinski, and A. M. Oleś, Origin of the Verwey transition in magnetite: Group theory, electronic structure, and lattice dynamics study, Phys. Rev. B **76**, 165124 (2007).

[33] H. Seo, M. Ogata, and H. Fukuyama, Aspects of the Verwey transition in magnetite, Phys. Rev. B **65**, 085107 (2002).

[34] G. Travaglini, I. Mörke, and P. Wachter, CDW evidence in one-dimensional $K_{0.3}MoO_3$ by means of Raman scattering, Solid State Commun. **45**, 289 (1983).

[35] R. Merlin, Generating coherent THz phonons with light pulses, Solid State Commun. **102**, 207 (1997).

[36] T. E. Stevens, J. Kuhl, and R. Merlin, Coherent phonon generation and the two stimulated Raman tensors, Phys. Rev. B **65**, 144304 (2002).

[37] A. Bruce, W. Taylor, and A. Murray, Precursor order and Raman scattering near displacive phase transitions, J. Phys. C: Solid State Phys. **13**, 483 (1980).

[38] See Supplemental Material at http://link.aps.org/supplemental/10.1103/PhysRevB.96.104308 for the characterization of our sample, the complete data sets of our pump-probe experiments as a function of temperature, the complementary data from our spontaneous Raman scattering experiments, our SVD analysis, and our complete *ab initio* calculations of optical constants and RMEs.

[39] A. Mann, E. Baldini, A. Tramontana, E. Pomjakushina, K. Conder, C. Arrell, F. van Mourik, J. Lorenzana, and F. Carbone, Probing the electron-phonon interaction in correlated systems with coherent lattice fluctuation spectroscopy, Phys. Rev. B **92**, 035147 (2015).

[40] B. Mansart, J. Lorenzana, A. Mann, A. Odeh, M. Scarongella, M. Chergui, and F. Carbone, Coupling of a high-energy excitation to superconducting quasiparticles in a cuprate from coherent charge fluctuation spectroscopy, Proc. Natl. Acad. Sci. USA **110**, 4539 (2013).

[41] K. Parlinski, Z. Q. Li, and Y. Kawazoe, First-Principles Determination of the Soft Mode in Cubic ZrO_2, Phys. Rev. Lett. **78**, 4063 (1997).

[42] K. Parlinski, software PHONON (Kraków, Poland, 2013).

[43] P. E. Blöchl, Projector augmented-wave method, Phys. Rev. B **50**, 17953 (1994).

[44] J. P. Perdew, K. Burke, and M. Ernzerhof, Generalized Gradient Approximation Made Simple, Phys. Rev. Lett. **77**, 3865 (1996).

[45] G. Kresse and J. Furthmüller, Efficient iterative schemes for *ab initio* total-energy calculations using a plane-wave basis set, Phys. Rev. B **54**, 11169 (1996).

[46] A. I. Liechtenstein, V. I. Anisimov, and J. Zaanen, Density-functional theory and strong interactions: Orbital ordering in Mott-Hubbard insulators, Phys. Rev. B **52**, R5467 (1995).

[47] P. Giannozzi, S. Baroni, N. Bonini, M. Calandra, R. Car, C. Cavazzoni, D. Ceresoli, G. L. Chiarotti, M. Cococcioni, I. Dabo *et al.*, QUANTUM ESPRESSO: A modular and open-source software project for quantum simulations of materials, J. Phys.: Condens. Matter **21**, 395502 (2009).

[48] A. Marini, C. Hogan, M. Grüning, and D. Varsano, Yambo: An *ab initio* tool for excited state calculations, Comput. Phys. Commun. **180**, 1392 (2009).

[49] P. Lee, T. Rice, and P. Anderson, Conductivity from charge or spin density waves, Solid State Commun. **14**, 703 (1974).

[50] P. M. Chaikin and T. C. Lubensky, *Principles of Condensed Matter Physics* (Cambridge University Press, Cambridge, UK, 2000).

[51] M. Cardona, *Light Scattering in Solids II: Basic Concepts and Instrumentation* (Springer, New York, 1982), Vol. 50.

[52] S. Borroni *et al.*, Mapping the lattice dynamical anomaly of the order parameters across the Verwey transition in magnetite, New J. Phys. (to be published).